

Experimental Sensing and Density Functional Theory Study of H₂S and SOF₂ Adsorption on Au-Modified Graphene

Xiaoxing Zhang,* Lei Yu, Xiaoqing Wu, and Weihua Hu

A gas sensor is used to detect SF₆ decomposed gases, which are related to insulation faults, to accurately assess the insulated status of electrical equipment. Graphene films (GrF) modified with Au nanoparticles are used as an adsorbent for the detection of H₂S and SOF₂, which are two characteristic products of SF₆ decomposed gases. Sensing experiments are conducted at room temperature. Results demonstrate that Au-modified GrF yields opposite responses to the tested gases and is thus considered a promising material for developing H₂S- and SOF₂-selective sensors. The first-principles approach is applied to simulate the interaction between the gases and Au-modified GrF systems and to interpret experimental data. The observed opposite resistance responses can be attributed to the charge-transfer differences related to the interfacial interaction between the gases and systems. The density of states and Mulliken population analysis results confirm the apparent charge transfer in Au-modified GrF chemisorption, whereas the van der Waals effect dominates the pristine graphene adsorption systems. Calculation results can also explicate the significant SOF₂ responses on Au-modified GrF. This work is important in graphene modulation and device design for selective detection.

1. Introduction

Sulfur hexafluoride (SF₆) is widely used in gas-insulated electrical equipment because it features excellent insulating and arc-extinguishing properties. At the early stages of insulation degradation of electrical equipment, the occurrence of partial

discharge (PD) causes the decomposition of SF₆ into various products, such as H₂S, SO₂, SOF₂, and SO₂F₂.^[1] These products can accelerate PD evolution in reverse, resulting in sharp reduction in the insulation strength of electrical equipment and formation of insulation faults. The composition and content of these decomposed components must be determined to identify the types, severities, and factors affecting PD and accurately assess the insulation status of electrical equipment.^[2–5] Gas sensors are used to detect the composition and content of SF₆ decomposed gases.^[6]

Graphene is a promising material for various applications, such as energy storage,^[7] nanoelectronic devices,^[8] fuel cells,^[9] and capacitors,^[10] because it features very high electron mobility caused by linear dispersion relation in the band structure of the π and π^* states around the Dirac point in the Brillouin zone.^[11] Gra-

phene sheets have been increasingly used as transducers since the first successful attempt to apply graphene for chemical sensing and detection of single-gas molecular absorption and desorption on graphene platforms.^[12] Experimental and theoretical studies have been conducted to elucidate the related gas adsorption mechanism. Nevertheless, previous studies mainly focused on common gaseous molecules, such as NH₃,^[13] NO₂,^[14,15] and CO₂.^[16]

Graphene sheets are functionalized with metals, chemical treatments, or other modifiers to enhance the chemisorption and selectivity of graphene to target gases.^[17,18] Doping metallic nanoparticles is a practical method for tuning the electronic structure of graphene sheets without significantly losing mobility. The reduced graphene oxide (rGO) sensors doped with Pd by spin coating,^[19] layer-by-layer (LBL) deposition,^[20] or chemical vapor deposition^[21] are used as functional films for hydrogen detection. Density functional theory (DFT) calculations further revealed that metal embedded and structural defects on graphene can effectively tune the electron density and transport properties of this carbon. In particular, Au- and Fe-embedded graphene have been used to enhance the chemical reactivity of graphene for potential applications in catalysts and gas sensing.^[22]

In this study, we used Au-modified graphene films (Au-modified GrF) as gas sensors for the detection of H₂S and SOF₂. Low-cost and simple LBL deposition was adopted in device

Prof. X. Zhang, L. Yu, Prof. X. Wu
State Key Laboratory of Power Transmission
Equipment and System Security and New Technology
Chongqing University
No.174 in Shazheng Street
Shapingba District, Chongqing 400044, P.R. China

Prof. X. Zhang
School of Electrical Engineering
Wuhan University
No.16 in Luojiashan Road
Wuchang District, Wuhan, Hubei Province 430072, P.R. China
E-mail: xiaoxing.zhang@outlook.com

Prof. W. Hu
Institute for Clean Energy and Advanced Materials
Southwest University
Chongqing 400715, P.R. China

This is an open access article under the terms of the Creative Commons Attribution License, which permits use, distribution and reproduction in any medium, provided the original work is properly cited.

DOI: 10.1002/adv.201500101



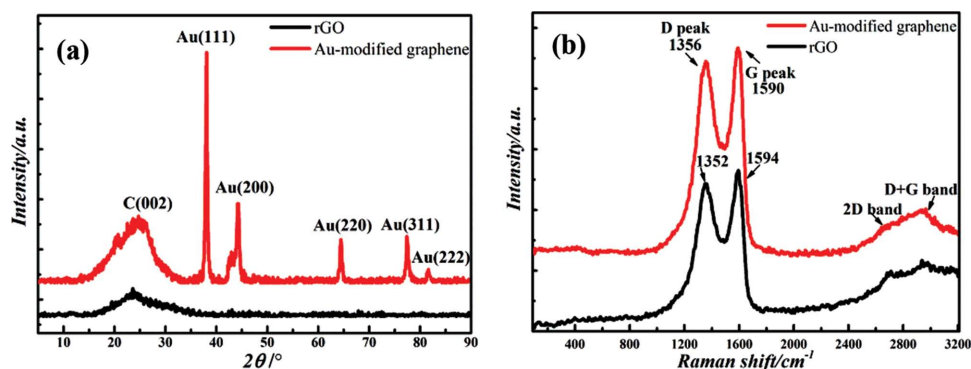


Figure 1. a) XRD patterns and b) Raman spectra of rGO and Au-modified GrF.

fabrication to investigate H_2S and SOF_2 adsorption responses. Based on first-principles calculations, we studied the interaction mechanism of the Au-modified GrF substrate with the gases. To the best of our knowledge, theoretical study combined with experimental data regarding the SOF_2 adsorption effect on Au-modified GrF has not been conducted and a thorough study of H_2S adsorption effect is rarely reported.

2. Results and Discussion

2.1. Experimental Sensing Performance

Materials must be thoroughly analyzed before the investigation of sensing performance. **Figure 1a** presents the XRD patterns of Au-modified GrF and rGO. The Au characteristic peaks in Au-modified GrF are located at 38.1° (111), 44.3° (200), 64.5° (220), 77.55° (311), and 81.65° (222), whereas the standard Au peaks at 38.184° (111), 44.392° (200), 64.576° (220), 77.547° (311), and 81.721° (222). The main Au (111) peak suggests the formation of a crystal phase, and the broad Au peaks imply that Au nanoparticles (AuNPs) are highly dispersed in the sample. The particle size of 14 nm was estimated from the main peak width of Au (111) through the Scherrer formula. The broad diffraction peaks at 24.63° and 23.77° for Au-modified GrF and rGO samples, respectively, reveal the carbon structure of graphene.

Raman spectra were determined for structural characterization.^[23] The typical post-subtraction Raman spectra were directly recorded on the sensor substrate and shown in **Figure 1b**. As the epoxy layers underlying the films function as insulators, the effect on electron distribution is disregarded. The comparison of the Raman spectra between Au-modified GrF and pure rGO films indicates that low amounts of modified AuNPs do not significantly change the formation of the

in-plane sp^2 domains in graphene. The Raman spectra of the films show the representative peaks at ≈ 1356 (D) and $\approx 1590 \text{ cm}^{-1}$ (G) and the broad bands between 2400 and 3200 cm^{-1} .^[20] As the intensity ratios of the D and G peaks are highly sensitive to the quality of material,^[24] we speculate that graphene-based

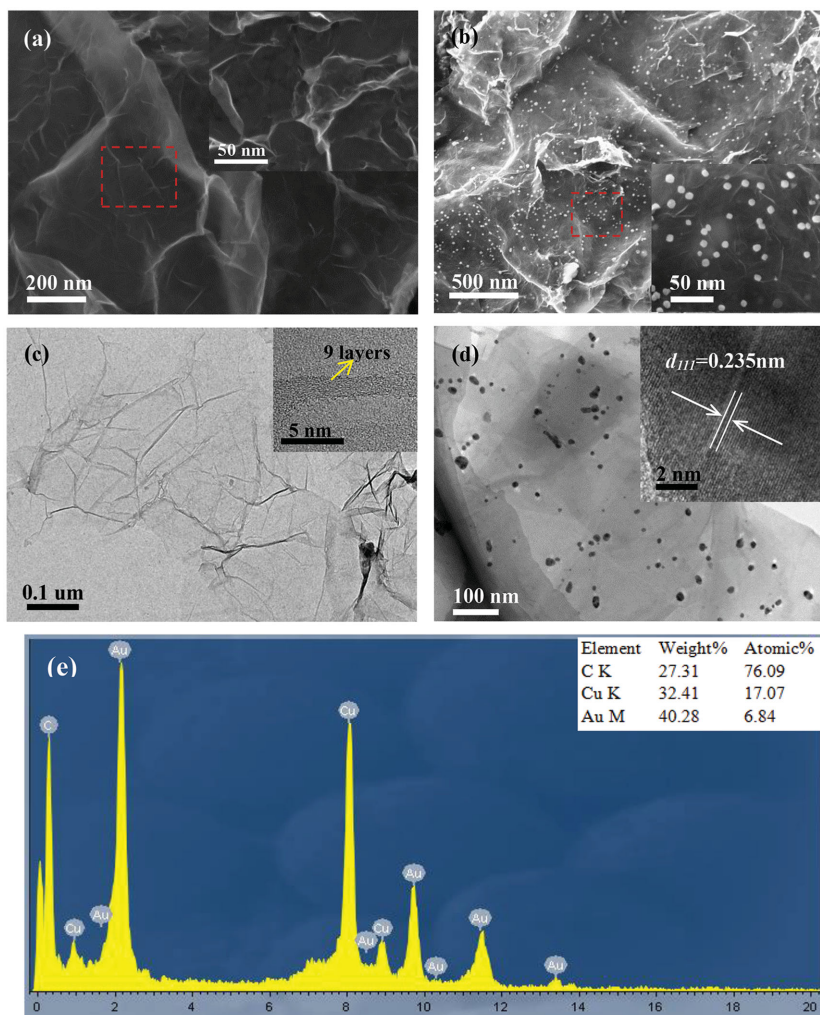


Figure 2. a) SEM image of rGO, b) SEM image of Au-modified GrF, c) TEM and HRTEM images (inset) of rGO, d) TEM and HRTEM images (inset) of Au-modified GrF, and e) EDS spectrum of Au-modified GrF.

materials contain multiple layers. Furthermore, the D peak is relatively pronounced, indicating the presence of a significant number of defects and a degree of confusion structure caused by deprivation of oxygen functionalities during hydrogen reduction.^[25] The sample flakes present a size of tens nanometers based on the D/G ratio of 0.85 and the G peak position. This observation is consistent with the results of XRD analysis.

Figure 2a shows low- and high-resolution SEM images of pure rGO. The clear and bright vision of rGO film sample indicates good electrical conductivity, which is free of metal spraying treatment. The flimsy, wrinkled, and fluctuant surface of two-dimensions is the typical morphology of rGO in practice application. Morphological structure, particle size, and metal dispersion of Au-modified GrF were also determined and the results are illustrated in Figure 2b. The enhanced area caused by highly dispersed AuNPs provides more available active sites on the sensing surface. AuNPs are uniformly embedded and covered on rGO. After analyzing several images, the average diameter of AuNPs is determined as tens of nanometers; this

finding is in agreement with the results of XRD and Raman studies. Figure 2c,d shows the TEM morphologies of pure rGO and Au-modified GrF, respectively. The rGO sample is with good light transmittance and obvious fold boundary. These features indicate that the quality of rGO sample is excellent, which owns few carbon layers. The specific number regarding these carbon layers is further confirmed to nine by HRTEM, which is embedded in Figure 2c. Therefore, our rGO sample is classified as the multilayer graphene. From the TEM image in Figure 2d, we confirm that AuNPs with dozen nanometer sizes are homogeneously dispersed on the rGO sheet surface. The HRTEM images in the inset in Figure 2d reveal the well-defined lattice fringes of Au (111) with a clear lattice distance ($d_{111} = 0.235$ nm), indicating that AuNPs exist and are highly crystalline. The EDS spectrum further verifies that Au is successfully modified in graphene.

XPS spectra are important in valence analysis. Figure 3 shows the XPS spectra of rGO and Au-modified GrF. The results reveal that $\approx 6\%$ AuNPs are successfully modified on the

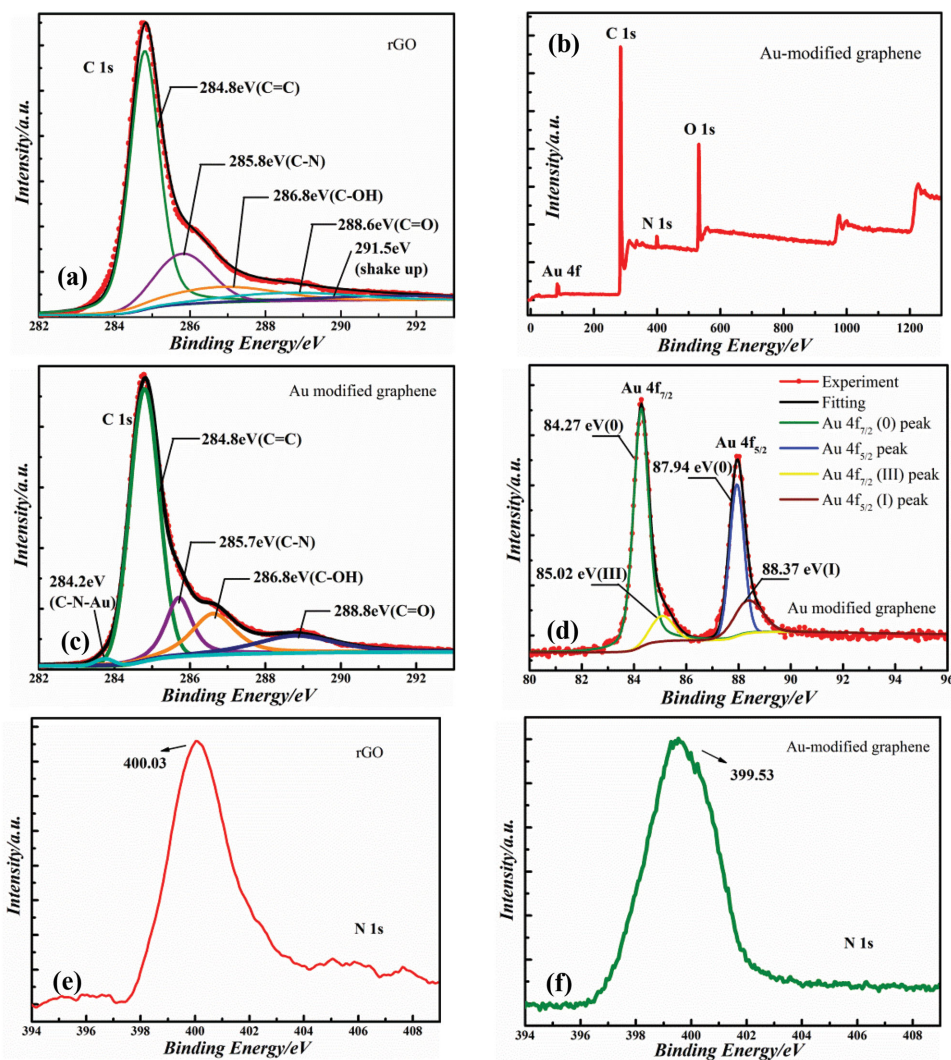


Figure 3. XPS spectra of a) C 1s region of rGO, b) Au-modified GrF, c) C 1s region of Au-modified GrF, d) Au 4f region of Au-modified GrF, e) N 1s region of rGO, and f) Au-modified GrF.

graphene surface, which is in accordance with the XRD, SEM, and TEM results. The high-resolution C 1s XPS spectrum of rGO indicates that numerous heteroatom defects exist on the plane and edges.^[26] Moreover, the C 1s spectrum can be fitted into four peaks corresponding to C atoms from four functional groups: nonoxygenated ring C at 284.8 eV, C in the C—N bond at 285.8 eV, hydroxyl C at 286.8 eV, and carbonyl C at 288.6 eV. After Au was introduced, a new peak appears at 284.2 eV and this peak is attributed to the C—N—Au bond.^[26–28] After peak-differentiation-imitating analysis, the Au 4f doublet deconvolutes into two pairs of peaks, which correspond to the reduced Au (0) at 84.27 eV in Au 4f_{7/2} and at 87.94 eV in Au 4f_{5/2}, Au (III) ions at 85.02 eV in Au 4f_{7/2} and Au (I) ions at 88.37 eV in Au 4f_{5/2}, respectively.^[29] Approximately 0.6 eV redshift of the XPS peak of Au (0) ions exists in Au 4f_{7/2}. This shift in the bonding energy may be ascribed to the substrate and reduced core-hole screening in metal particles. Furthermore, a dynamic electron transfer from modified AuNPs to the supported graphene films is confirmed by the existence of positively charged Au (III) and Au (I) ions according to the electrostatic balance principle and theoretical calculation in DFT study. Moreover, according to the N 1s spectra of rGO and Au-modified sample in Figure 3e,f, modified AuNPs result in a blue shift of binding energy (from 400.03 eV to 399.53 eV), which indicates that Au-modified sample is a covalent hybrid based on the coordination or chemical effects between heteroatoms, such as, N and O, and Au clusters.^[26,30,31]

Target gas molecules, namely, H₂S and SOF₂, were delivered to the graphene-based sensor device through mass flow-controlled dilution with clean, pure, and dry helium. Figure 4a–d represents the responses of the rGO and Au-modified GrF

sensors in terms of resistance changes during exposure to varied concentrations of target gases in an autonomous sealed chamber. Resistance change is defined as

$$\Delta R = R_F - R_i \quad (1)$$

where R_F represents the sensor resistance at the final target gas exposure and R_i represents the initial vacuum resistance at the previous rest period. Sensor response^[32] is universally defined as

$$\text{Sensitivity} = \frac{\Delta R}{R_i} \times 100\% \quad (2)$$

Although humidity and temperature significantly affect the sensor response, specific operating conditions in electrical equipment may reduce this variation. Figure 4a–d shows the sensor responses after exposure to 50 and 100 ppm of H₂S and SOF₂. Only the responses associated with these two concentrations were analyzed to investigate the sensing mechanism. For rGO under ambient conditions, 100 and 50 ppm H₂S cause 15.78% and 10.53% reduction in resistance, respectively. SOF₂ is not sensitive to rGO. Moreover, 100 and 50 ppm SOF₂ result in 23.83% and 15.36% reduction in the resistance of Au-modified GrF, respectively. These findings indicate that Au-modified GrF exhibits higher sensitivity to SOF₂ than rGO. Although Au-modified GrF is also sensitive to H₂S, a positive resistance change was observed. In this system, 100 and 50 ppm H₂S increase the resistance by 28.15% and 18.73%, respectively. These sensing performances reveal that the Au-modified GrF and pure rGO sensors are promising materials for selective detection. Therefore, the sensing behavior was further analyzed.

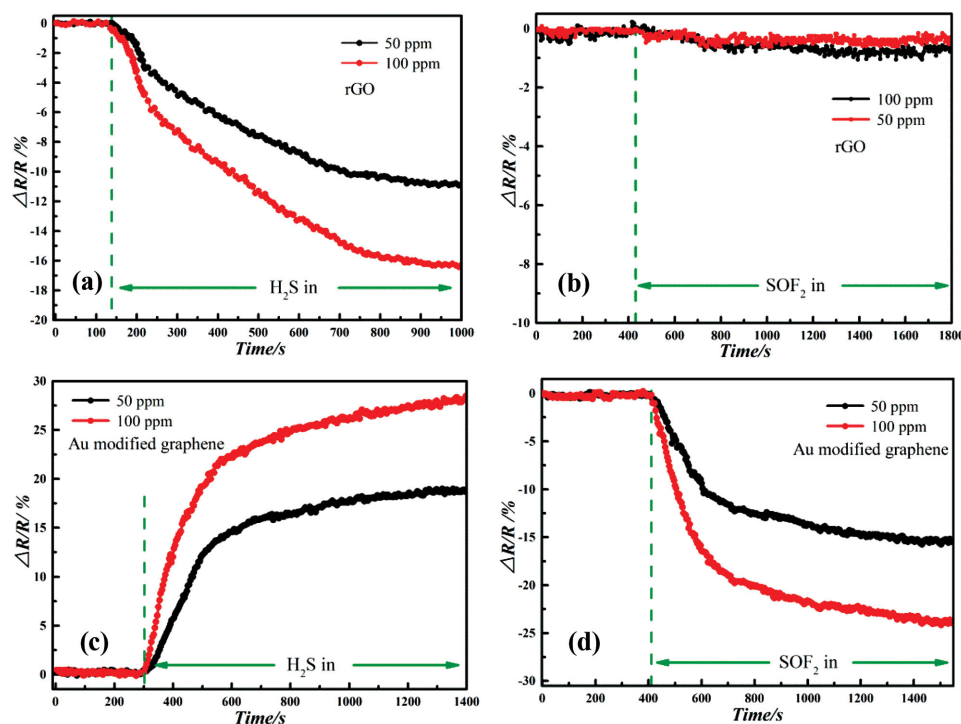


Figure 4. Experimental transient responses of rGO sensors to a) H₂S and b) SOF₂, and Au-modified GrF sensors to c) H₂S and d) SOF₂.

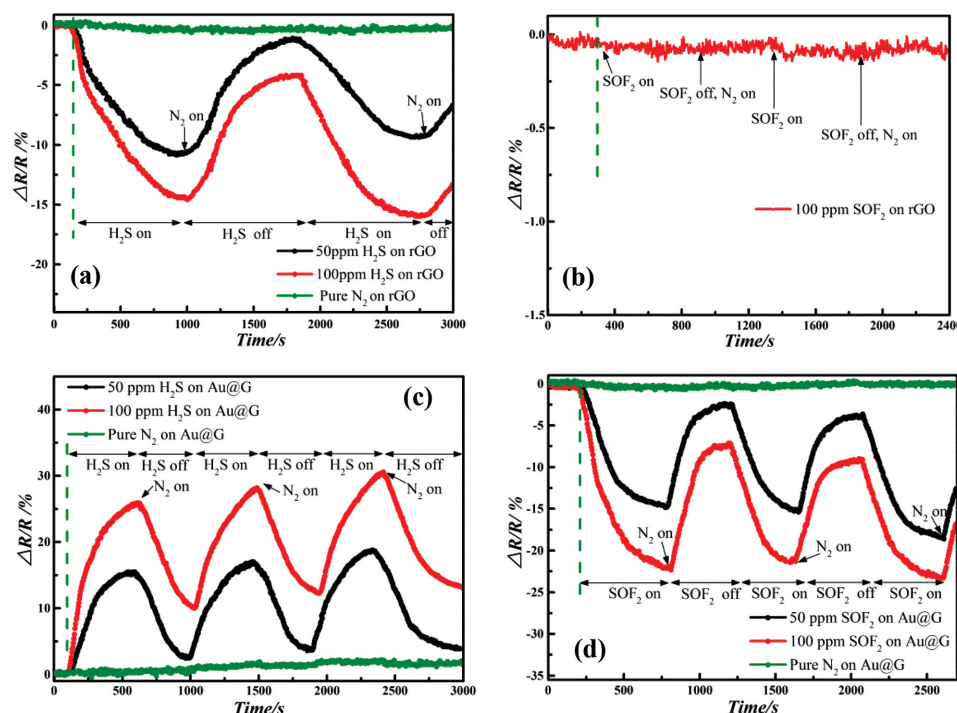


Figure 5. Transient responses of rGO sensors to a) H_2S , b) SOF_2 flows, and Au-modified GrF sensors to c) H_2S , d) SOF_2 flows.

Further experiments were performed to determine the response properties under repeated gas pulses. For this, a series of sensing experiments involving H_2S and SOF_2 were performed at the same setting. **Figure 5a,b** shows our rGO sensor's behavior in repeated H_2S and SOF_2 flows, respectively, and **Figure 5c,d** illustrates the responses of our Au-modified GrF sensor to target gases. The target gas and pure N_2 were flown over the sensor sequentially and recurrently, and the changes in resistance were measured. N_2 flow expelled the target gas that had already been existed, for the purpose of exploring its recovery property and preparing the next detection round at the same time. Based on the results in **Figure 5**, the sensor response presents the similar variation tendency in comparison with the single test result, regardless of the magnitude and response direction. In addition, we have noticed that the transient for H_2S on rGO sensor is much slower compared to the response behavior on Au-modified GrF. Hence, the response speed of Au-modified GrF is proved to be better than pure rGO.

2.2. DFT Study of Adsorption Mechanism

2.2.1. Au-Modified Graphene

A simulation model was constructed for theoretical calculation to investigate the factors affecting sensor performance and the sensing mechanism. We already discussed the nature of the bonding between decorated Au and graphene. The three possible positions^[22] considered are the top site above a carbon atom (T), bridge site between the C—C bond

(B), and hollow site at the hexagon center (H), which are illustrated in **Figure 6a**. Our calculation results show that the T site model holds the lowest energy, as shown in **Figure 6b**. And the detailed calculated energy information has been summarized in Table S1 (Supporting Information). Therefore, our calculation focuses on the T position, in which Au substitutes C. Au atoms in Au-modified GrF adopt a partial sp^3 configuration and protrude from the graphene plane by 1.87 Å along the Z axis. The bond lengths (2.07 Å) of the three C—Au bonds confirm the partial sp^3 configuration of Au atoms. A similar bonding geometry was observed in M-modified graphene ($M = \text{Pd}$, Pt , and Mn)^[33–35] from previous PBE calculations. In the present calculation, the electrons on Au are depleted when Au bonded to C atoms. This observation is in agreement with the presence of positively charged Au (I) and Au (III) ions in the XPS analysis. The spin-polarized density of states (DOS) of Au-modified GrF and pristine graphene are illustrated in **Figure 7a**. Au instigates finite DOS and introduces an evident conductance change

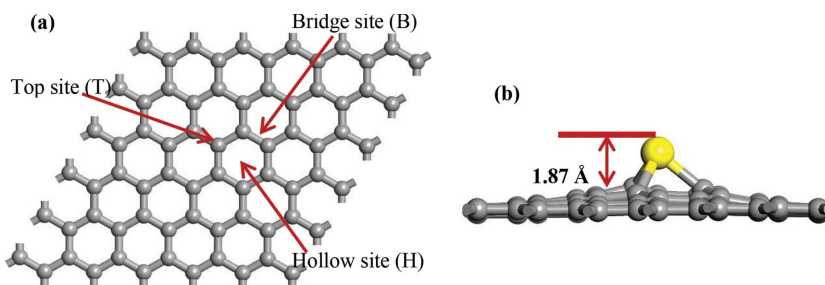


Figure 6. a) Three possible modification positions of Au atom on graphene. b) Side view of partial atomic structure for T site modification model.

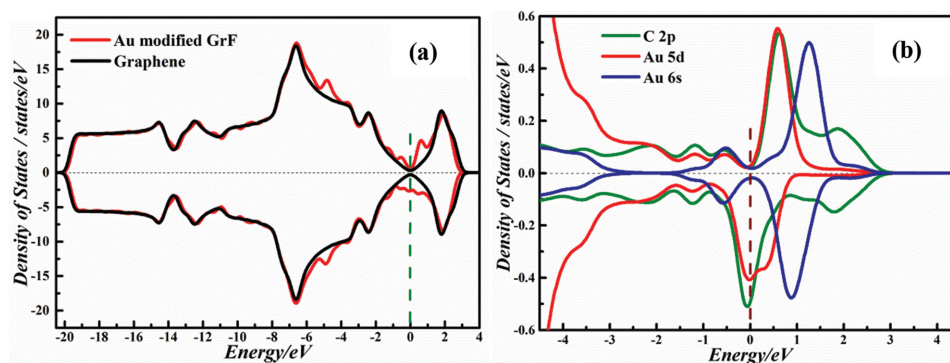


Figure 7. a) Spin-polarized DOS of pristine graphene (black curve) and Au-modified GrF (red curve) and b) PDOS projected on the s orbital (blue curve) and d orbital (red curve) of Au and 2p orbital (green curve) of neighboring C.

near the Fermi level to pristine graphene, indicating that the presence of Au endows the zero-gap material with a metallic property. Moreover, Au breaks the symmetry between spin-up and spin-down channels and generates a magnetic moment ($-1.005 \mu_B$). According to the partial DOS (PDOS) in Figure 7b, magnetic moments mainly originate from the depleted spin-down electrons of the d orbital of Au and the p orbital of the neighboring C.

2.2.2. Gas Adsorption Effects

Different orientations are required to achieve the most stable adsorption configuration, which exhibits the lowest total energy and highest adsorption energy.^[36] Figure 8 illustrates the most stable adsorption configurations of single and double H_2S and SOF_2 molecules on Au-modified GrF. Table 1 presents the calculated results of every adsorption system. Figure 9 further shows the spin-polarized DOS for H_2S and SOF_2 adsorption systems. We focused on the adsorption effects of double molecules on the Au-modified GrF plane according to previous research, which reported that several molecule adsorption cases were inclined to be unstable at room temperature because of significant decreases in their E_{ad} .^[22] Although part of Au concentration was ignored in DFT calculation, we aimed to establish the basic principle by using a simple model. The influence

of Au concentration on the mechanisms underlying sensing properties was further investigated.

H_2S Adsorption Cases: In the Au-modified GrF- H_2S system, H_2S is adsorbed parallel to the surface with S atoms closest to Au. The geometric structure of H_2S slightly changes as the H—S—H bond angle (91.181°) expands to 91.719° and the H—S bond angle (1.356°) extends to 1.360 and 1.362 Å. H_2S molecules also prefer a closer configuration on the Au-modified GrF plane than that on the pristine graphene, as indicated by the shorter distance between Au-modified graphene and S (2.401 Å) than that between pristine graphene and H_2S (3.108 Å). Hence, H_2S molecules are chemisorbed on Au-modified GrF as evidenced by the high adsorption energy (-0.9 eV) and electron transfer ($0.348 e$) from H_2S molecules to Au-modified GrF. This electron transfer leads to electron enrichment on the Au-modified GrF surface. In graphene- H_2S adsorption case, the obtained electron transfer value ($0.011 e$) indicates the presence of few electron interactions. Nevertheless, the adsorption energy of graphene- H_2S (-0.617 eV) presents a relatively strong intermediate between physisorption and chemisorption,^[37,38] which indicates the prevalence of van der Waals. By comparing the studies on Au-modified GrF- H_2S and pure Au-modified GrF, we observed an evident difference in DOS near the Fermi level, indicating a decrease in the surrounding DOS. For Au-modified GrF, the Fermi level shifts upward by

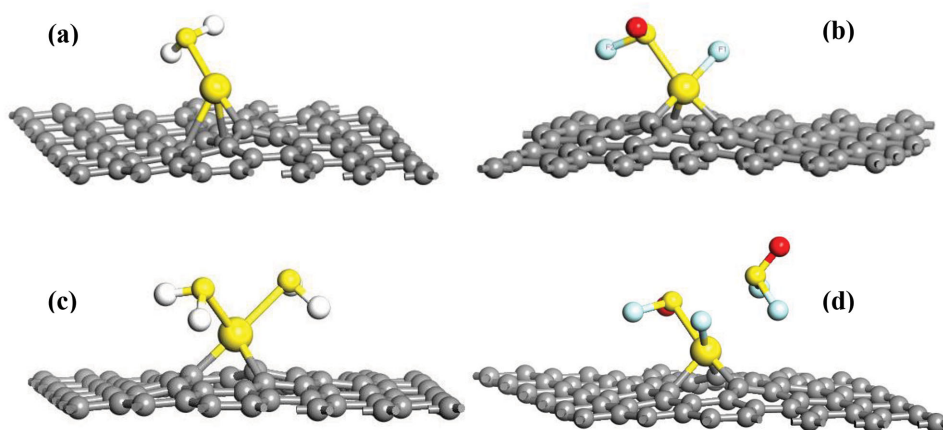


Figure 8. Optimized configurations of single a) H_2S , b) SOF_2 , c) $2H_2S$, and d) $2SOF_2$ adsorbed on Au-modified GrF.

Table 1. Adsorption parameters in single- and double-target molecule cases.

Configuration	$d_1^a)$ [Å]	$d_2^a)$ [Å]	$E_{ad}^b)$ [eV] (with DFT-D)	$Q_{t1}^c)$ [e]	$Q_{t2}^c)$ [e]
Graphene-H ₂ S	3.108		−0.617	+0.011	
Au-modified GrF-H ₂ S	2.401		−0.900	+0.348	
Au-modified GrF-2H ₂ S	2.593	2.598	−1.718	+0.304	+0.302
Graphene-SOF ₂	3.526		−0.267	−0.002	
Au-modified GrF-SOF ₂	2.039		−0.961	−0.624	
Au-modified GrF-2SOF ₂	2.519	3.970	−1.334	−0.658	−0.031

^{a)} D denotes the shortest distance between the molecule and the oriented substrate, where d_1 and d_2 represent former and latter molecules, respectively; ^{b)} E_{ad} describes the surface interaction $E_{\text{molecule/AuNPs@graphene}} - E_{\text{molecule}} - E_{\text{AuNPs@graphene}}$; ^{c)} Q_t represents the net charge transformation, which indicates the redistribution charges in the adsorption system, where Q_{t1} and Q_{t2} refer to former and latter molecules, respectively.

0.043 eV, which is reminiscent of an n-type effect caused by adsorbed H₂S molecules. The magnetic moment further changes to 0.999 μ_B .

We found that the two H₂S molecules exhibiting a similar configuration are the stable configuration on Au-modified GrF; in this configuration, each S atom moves closer to Au. The binding geometry is similar to that of the Au-modified GrF-H₂S system. The adsorption energy (−1.718 eV) is two times higher than that of Au-modified GrF-H₂S. Although ≈ 0.3 electrons per H₂S molecule transfer to the Au-modified GrF complex in the Au-modified GrF-2H₂S system, the system still exhibits an n-type sensing nature. The n-type effect introduced by the two H₂S cases could be attributed to the upward shift of the Fermi level by 0.077 eV. This observation is also consistent with the higher adsorption energy of 2H₂S on Au-modified GrF than 1H₂S. In fact, our separate PDOS calculation confirms that Au prefers to hybridize S atoms in the H₂S valence band, which contributes to the strong interaction between Au and adsorbed H₂S. A comparison study using Figure 9a suggests that 2H₂S adsorption remains magnetic in the semiconductor system with a magnetic moment of 0.823 μ_B .

SOF₂ Adsorption Cases: In the Au-modified GrF-SOF₂ case, SOF₂ prefers the configuration in which SOF₂ is located above Au-modified GrF; in this configuration, S and F atoms bond to Au as indicated by the distance between S and Au (2.508 Å) and F and Au (2.039 Å). The F–S bond extends longer (2.894 Å) than that in the gas phase (1.668 Å) because of the charge transfer, indicating SOF₂ rupture. The results of Mulliken population analysis confirm the occurrence of a significant electron transfer (0.624 e) from Au-modified GrF to SOF₂; this phenomenon features a p-type process with SOF₂ as an acceptor. The adsorption energy (−0.961 eV) is similar to that in the Au-modified GrF-H₂S case. Our DOS calculation results further reveal that the spin-up and spin-down channels shift downward by 1.05 eV, indicating the strong p-type effect of SOF₂ adsorption. The adsorbed SOF₂ converts the system of Au-modified GrF from magnetic metal into a nonmagnetic system with magnetic moment quenching. This observation differs from that in the H₂S cases, which maintains the magnetic property.

When two SOF₂ molecules move closer to Au-modified GrF, the most stable configuration is where one SOF₂ prefers the active state and approaches the Au-modified GrF plane and the other SOF₂ moves away from Au-modified GrF (Figure 8d). The inactive SOF₂ does not effectively participate in the interaction process as also confirmed by the results of Mulliken population analysis. Approximately 0.658 electrons transfer to the active SOF₂, whereas 0.031 electrons transfer to the inactive site. Minimal change is introduced to the DOS around the Fermi level (the overlapping solid black and red curves) because of the inactive SOF₂. In the H₂S case, this observation differs from that in 2H₂S adsorption, in which one H₂S exhibits equivalent effect to the other H₂S. The adsorption energy of the Au-modified GrF-2SOF₂ system (−1.334 eV) is higher than that in Au-modified GrF-SOF₂ (0.961 eV). The small amounts of additional energy can be ascribed to the van der Waals interaction, which is supplemented by electrostatic effect caused by chemically inactive SOF₂ molecules. The results of DOS analysis further indicate that the Fermi level shifts downward by 0.966 eV compared with that of Au-modified GrF; this phenomenon demonstrates a p-type effect. Moreover, Au-modified GrF-2SOF₂ case maintains its nonmagnetic property similar to the Au-modified GrF-SOF₂ system.

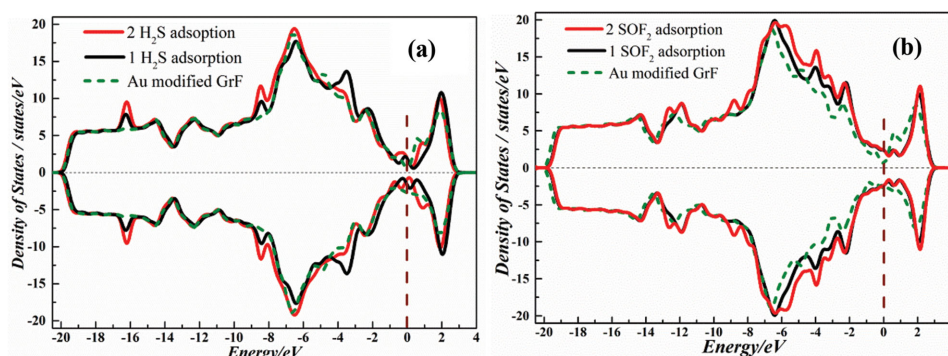


Figure 9. a) Spin-polarized DOS of Au-modified GrF (dash olive curve), Au-modified GrF-H₂S (solid black curve), and Au-modified GrF-2H₂S (solid red curve). b) Spin-polarized DOS of Au-modified GrF (dash olive curve), Au-modified GrF-SOF₂ (solid black curve), and Au-modified GrF-2SOF₂ (solid red curve). The Fermi energy is set as $E - E_F$.

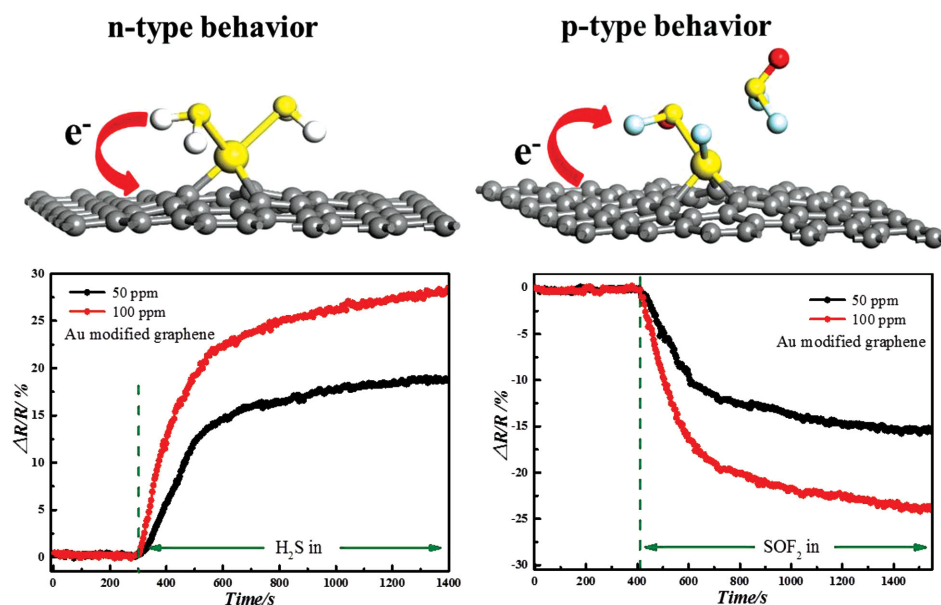


Figure 10. Correlation between sensing performance and nature of carriers for Au-modified GrF.

2.2.3. Discussion of Sensing Performances Based on DFT Calculations

Figure 4a,c presents the responses of H_2S , which is significantly sensitive to rGO and Au-modified GrF but exhibits opposite effect compared with each other. As confirmed in our DFT calculations, the pronounced chemisorption effect contributes to the H_2S responses on Au-modified GrF. However, the results also prove that the adsorption interaction with pure graphene is typical physisorption, which contradicts the experimental findings. The factors affecting this discrepancy remain unclear, but we postulate that it could be related to the method used to manufacture pure graphene films. The pure graphene films used in this study were prepared through chemical reduction, which could inevitably harbors heteroatoms, such as N and O. The combined XPS analysis results and Raman spectra reveal the presence of nonoxygenated ring, C–N bonds, hydroxyl C, and carbonyl, which may affect the sensing interaction. This phenomenon must be further investigated through theoretical and experimental studies.

For SOF_2 , sensing experiments were conducted on pure graphene and Au-modified GrF (Figure 4b,d) to investigate the influence of decorated Au on gas sensing. The sensing performance of SOF_2 on pure graphene is not significant as it only results in 0.7% decrease in resistance. This response is significantly lower than that of Au-modified GrF, which decreases the resistance by a maximum of 23.83%. In DFT calculations, the interaction between SOF_2 and Au-modified GrF is chemisorption as evidenced by the charge transfer from Au-modified GrF to SOF_2 (0.624 e in the Au-modified GrF- SOF_2 system). This finding could also be attributed to the higher chemical potentials of Au-modified GrF than the lowest unoccupied molecular orbital of SOF_2 . Nevertheless, as SOF_2 is physisorbed on the pure graphene surface, no charge transfer (Table 1) could occur. This physisorption phenomenon, in which only the van der Waals effect dominates, could contribute to the unclear

responses of SOF_2 on pure graphene. In addition, the calculated adsorption energy (–0.267 eV) is not significant in the graphene- SOF_2 system compared with that in the Au-modified GrF- SOF_2 system (–1.334 eV). Therefore, based on our experiment and calculation results, we successfully established an effective approach to manufacture SOF_2 sensors.

Figure 4c,d presents the comparison between the performance of a resistive sensor with H_2S and the SOF_2 sensing results obtained using Au-modified GrF. Au-modified graphene exhibits a 28.15% increase in resistance for 100 ppm H_2S and 23.83% decrease in resistance after 12 min of exposure to 100 ppm SOF_2 . The fabricated Au-modified graphene sensor demonstrates a reverse resistance change because of gas species. The n-type and p-type behavior determined through the altered direction of the charge carrier plays a dominant role in the conduction response.^[39,40] Different conductivity types of graphene-based sensors were reported in previous experimental studies, but no specific trend was observed.^[38] Based on our DFT calculations, we infer that H_2S exhibits an n-type behavior with electron depletion on itself. An increase in resistance was further observed in the sensing experiment, indicating the n-type sensing nature of the Au-modified graphene layer. In DFT calculations, SOF_2 presents a p-type behavior with electron withdrawing capability, in which electrons can be removed from the adsorbent surface. This phenomenon results in decreased resistance, thereby confirming that Au-modified GrF displays a p-type sensing behavior. The corresponding correlation between sensing performance and nature of carriers for Au-modified GrF was obtained under our experiment conditions and illustrated in Figure 10.

3. Conclusions

Detection of H_2S and SOF_2 , which are two types of SF_6 decomposed gases, has gained importance because they are

significantly related to insulation faults in power equipment. As current detection methods suffer from online monitoring shortage, electrochemistry sensors could be a promising technology for online detection.

Pure graphene films and graphene films incorporated with AuNPs were fabricated as gas sensors through deposition–precipitation method. Sensing experiments conducted at room temperature demonstrated that Au-modified GrF is a promising material for developing H₂S and SOF₂ selective sensors because it yields opposite responses for these gases. The interaction between the Au-modified GrF surface and these gases was simulated through first-principles calculations. The results reveal that the opposite responses observed in experiments could be due to the charge-transfer differences related to the interfacial interaction within gases and Au-modified GrF systems. Calculation and experimental findings consistently show n-type H₂S functions as an electron donor and p-type SOF₂ as an electron acceptor.

The results of sensing experiments further show the strong response of the Au-modified GrF sensor for SOF₂. This finding confirms the robustness and the ability to adsorb SOF₂ of the sensor compared with the poor performance on pure graphene films. According to the results of DFT calculations, the typical chemisorption effect between decorated Au and SOF₂ could be the main reason for this observation and the adsorption of the pristine graphene corresponds to physisorption dominated by van der Waals.

Our calculation results further show that the H₂S chemisorption behavior endows Au-modified GrF with a magnetic system, whereas SOF₂ adsorption converts the system into a nonmagnetic one. This result may be utilized in designing novel magnetic sensing or switching devices, but requires further investigation through experimental methods.

4. Experimental Section

Experimental Details: Carboxyl functionalized graphene and rGO were purchased from XF NANO, Inc. (Nanjing, China). Dimethylformamide (DMF), acetone, and absolute ethyl alcohol were purchased from Huihuang Chemical Reagent Co., Ltd (Chongqing, China). NaBH₄ and HAuCl₄ were purchased from Aladdin Chemistry Co., Ltd. All chemicals in this work were of analytical grade and used without further purification, and double-distilled water was used throughout the experiments.

Au-modified GrF was synthesized through the following chemical reduction procedures.^[29] Carboxyl functionalized graphene (1 mg) was dispersed in HAuCl₄ (5 mL, 1×10^{-3} M) solution as a precursor under constant sonication for 40 min to reach a stable colloidal state. Briefly, NaBH₄ (5 mL, 40×10^{-3} M) solution was added dropwise to the colloid solution and the solution was vigorously stirred for 30 min. The solution was then subjected to centrifugal separation, and products were collected and washed with distilled water several times. The washed products were dried in a vacuum oven at 60 °C for 12 h to obtain Au-modified GrF. Au-modified GrF (5 mg) powder was ultrasonically dispersed in DMF solution (200 mL) for 30 min to achieve good dispersibility.

Sensors were fabricated using Au-modified GrF through LBL deposition.^[41] Responses were measured by monitoring surface resistance changes in a pressure-tight system. For the planar sensor depicted in **Figure 11**, copper electrodes were inter-digitally etched on epoxy resin with ≈ 30 μ m thick foil and 0.2 mm electrode gap. The prepared Au-modified GrF solution was continuously dispersed on the substrate and then dried until the desired initial surface resistance values, which translate to the formation of uniform, dense, and smooth

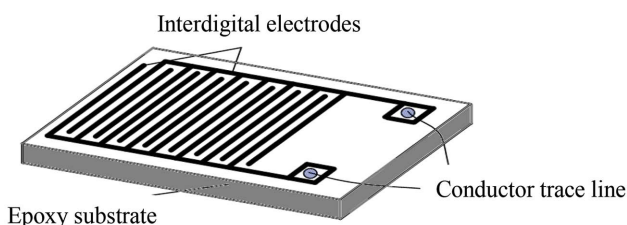


Figure 11. Schematic structural view of a planar sensor.

deposited films, were achieved. The fabricated Au-modified GrF sensor was used for detection. A sensing element was placed in an autonomous sealed chamber connected to an electrochemical analyzer. As the initial vacuum resistance stability is a prerequisite for gas detection experiment, responses were measured at room temperature and repeated several times to obtain reliable results.

X-ray diffraction (XRD) patterns were recorded on a Rigaku D/Max-1200X using Cu K α radiation ($\lambda = 0.15418$ nm) at 40 kV and 30 mA. Wide-angle XRD patterns were collected at a scanning speed of 10° per minute over the 2θ range of 5° to 100°. Raman spectra were determined using a Renishaw inVia Raman microscope configured with a 532 nm wavelength laser and full-range grating. Scanning electron microscopy (SEM) images were recorded with a Zeiss Auriga Focus Ion Beam/Field-Emission SEM dual-cross system operated at 30 kV and 2 nA. The samples were directly exfoliated from the planar sensor. High-resolution transmission electron microscopy (HRTEM) combined with energy dispersive spectroscopy (EDS) images was recorded with an FEI Tecnai G2 F20 S-TWIN operated at 200 kV. X-ray photoelectron spectroscopy (XPS) was performed on a Thermo ESCALAB 250Xi spectrometer with Al K α (1486.6 eV) radiation. All measurements were conducted under ambient condition.

Theoretical Methods: To determine the role of van der Waals, we performed theoretical calculations by using dispersion-corrected DFT (DFT-D) provided by the DMol³ code. The exchange and correlation energies included were identified through a generalized gradient approximation in revised Perdew–Burke–Ernzerhof (PBE) format.^[42–44] Core treatment, in which core electrons are replaced by a single effective potential, was conducted with DFT semi-core pseudopotentials to evaluate relativistic effects. To simulate a 2D graphene sheet, we modeled a supercell comprising 6×6 units (consisting of 72 atoms) in the XY plane. A vacuum region of 20 Å in the Z direction was also adopted to prevent the interaction between adjacent layers. The k -point mesh was increased to $6 \times 6 \times 1$ for the Brillouin-zone integration to obtain accurate results. All calculations were performed in a spin-unrestricted manner. The convergence tolerance of energy was set at 1.0×10^{-6} Ha in geometry optimization.

Supporting Information

Supporting Information is available from the Wiley Online Library or from the author.

Acknowledgements

This work was supported by the Basic Science Research Program through the National Natural Science Foundation of China (NSFC 51277188) and the research project of State Key Laboratory of Power Transmission Equipment & System Security and New Technology (No. 2007DA10512713207). Some additional computations were supported by the Theoretical Physics Institute of Chongqing University. The School of Chemistry and Chemical Engineering of Chongqing University, which supported some experimental instruments, is also appreciated.

Received: March 23, 2015
Revised: May 29, 2015
Published online: September 10, 2015

- [1] R. J. V. Brunt, J. T. Herron, *IEEE Trans. Dielectr. Electr. Insul.* **1990**, 25, 75.
- [2] G. C. Qing, G. Z. Qiao, C. Q. Yu, L. W. Xin, M. Chun, *Power Syst. Technol.* **2000**, 24, 1.
- [3] J. B. Jia, F. B. Tao, L. J. Yang, Q. G. Zhang, *Proc. CSEE* **2006**, 26, 106.
- [4] J. Tang, P. Z. Fu, Y. P. Jian, X. Z. Xiao, Y. Qiang, J. H. Jian, Z. H. Xing, *IEEE Trans. Dielectr. Electr. Insul.* **2013**, 20, 864.
- [5] J. Tang, F. Liu, X. X. Zhang, Q. Meng, J. Zhou, *IEEE Trans. Dielectr. Electr. Insul.* **2012**, 19, 29.
- [6] X. X. Zhang, Q. C. Chen, J. Tang, H. H. Wei, B. Z. Jin, *Sci. Rep.* **2014**, 4, 1.
- [7] H. W. Dong, K. Rong, W. C. Dai, G. Y. Zhen, M. N. Zi, L. Juan, V. S. Laxminkant, H. H. De, G. Z. Ji, L. G. Gordon, L. Jun, A. P. Michael, A. A. Ilhan, *ACS Nano* **2010**, 4, 1587.
- [8] B. Clarire, M. S. Zhi, B. L. Tian, B. L. Xue, Y. O. Asmeron, F. Rui, T. D. Zhen, N. M. Alexei, H. C. Edward, N. F. Phillip, A. H. Walt, *J. Phys. Chem. B* **2004**, 108, 19912.
- [9] L. Qu, Y. Liu, J. B. Baek, L. Dai, *ACS Nano* **2010**, 4, 1321.
- [10] El-M. F. Kady, V. Strong, S. Dubin, R. B. Kaner, *Science* **2012**, 335, 1326.
- [11] A. K. Geim, K. S. Novoselov, *Nat. Mater.* **2007**, 6, 183.
- [12] F. Schedin, A. K. Geim, S. V. Morozov, E. W. Hill, P. Blake, M. I. Katsnelson, K. S. Novoselov, *Nat. Mater.* **2007**, 6, 652.
- [13] Y. H. Zhang, Y. B. Chen, K. G. Zhou, C. H. Liu, J. Zeng, H. L. Zhang, Y. Peng, *Nanotechnology* **2009**, 20, 185504.
- [14] O. Leenaerts, B. Partoens, F. M. Peeters, *Phys. Rev. B* **2008**, 77, 125416.
- [15] T. O. Wehling, K. S. Novoselov, S. V. Morozov, E. E. Vdovin, M. I. Katsnelson, A. K. Geim, A. I. Lichtenstein, *Nano Lett.* **2008**, 8, 173.
- [16] A. Ghosh, K. S. Subrahmanyam, K. S. Krishna, S. Datta, A. Govindaraj, S. K. Pati, C. N. R. Rao, *J. Phys. Chem. C* **2008**, 112, 15704.
- [17] X. Huang, X. Qi, F. Boey, H. Zhang, *Chem. Soc. Rev.* **2012**, 41, 666.
- [18] C. Xu, X. Wang, J. Zhu, *J. Phys. Chem. C* **2008**, 112, 19841.
- [19] P. A. Pandey, N. R. Wilson, J. A. Covington, *Sens. Actuators B: Chem.* **2013**, 183, 478.
- [20] U. Lange, T. Hirsch, V. M. Mirsky, O. S. Wolfbeis, *Electrochim. Acta* **2011**, 56, 3707.
- [21] M. G. Chung, D. H. Kim, D. K. Seo, T. Kim, H. U. Im, H. M. Lee, J. B. Yoo, S. H. Hong, T. J. Kang, Y. H. Kim, *Sens. Actuators B: Chem.* **2012**, 169, 387.
- [22] M. Zhou, Y. H. Lu, Y. Q. Cai, C. Zhang, Y. P. Feng, *Nanotechnology* **2011**, 22, 385502.
- [23] G. Wang, J. Yang, J. Park, X. Gou, B. Wang, H. Liu, J. Yao, *J. Phys. Chem. C* **2008**, 112, 8192.
- [24] L. G. Cançado, A. Jorio, E. M. Ferreira, F. Stavale, C. A. Achete, R. B. Capaz, M. V. O. Moutinho, A. Lombardo, T. S. Kulmala, A. C. Ferrari, *Nano Lett.* **2011**, 11, 3190.
- [25] Y. Li, Y. Yu, J. G. Wang, J. Song, Q. Li, M. Dong, C. J. Liu, *Appl. Catal. B: Environ.* **2012**, 125, 189.
- [26] H. Yin, H. Tang, D. Wang, Y. Gao, Z. Tang, *ACS Nano* **2012**, 6, 8288.
- [27] Q. Mildred, S. Konstantinos, G. Marek, R. B. Wesley, R. Petra, P. Maurizio, *ACS Nano* **2010**, 4, 3527.
- [28] J. R. Michael, H. J. James, *J. Colloid Interface Sci.* **2007**, 310, 425.
- [29] Y. Hu, Z. Xue, H. He, R. Ai, X. Liu, X. Lu, *Biosens. Bioelectron.* **2013**, 47, 45.
- [30] Y. F. Jia, B. Xiao, K. M. Thomas, *Langmuir* **2002**, 18, 470.
- [31] J.-B. Wu, Y.-F. Lin, J. Wang, P. J. Chang, C. P. Tasi, C. C. Lu, H. T. Chiu, Y. W. Yang, *Inorg. Chem.* **2003**, 42, 4516.
- [32] S. Bai, T. Guo, Y. Zhao, J. Sun, D. Li, A. Chen, C. C. Liu, *Sens. Actuators B: Chem.* **2014**, 195, 657.
- [33] K. T. Chan, J. B. Neaton, M. L. Cohen, *Phys. Rev. B* **2008**, 77, 235430.
- [34] A. Pramanik, H. S. Kang, *J. Phys. Chem. C* **2011**, 115, 10971.
- [35] P. A. Khomyakov, G. Giovannetti, P. C. Rusu, G. Brocks, V. D. Brink, P. J. Kelly, *Phys. Rev. B* **2009**, 79, 195425.
- [36] R. Balog, B. Jørgensen, L. Nilsson, M. Andersen, E. Rienks, M. Bianchi, M. Fanetti, E. Lægsgaard, A. Baraldi, S. Lizzit, Z. Slijivancanin, F. Besenbacher, B. Hammer, T. G. Pefersen, P. Hofmann, L. Hornekær, *Nat. Mater.* **2010**, 9, 315.
- [37] P. Jena, *J. Phys. Chem. Lett.* **2011**, 2, 206.
- [38] Y. H. Zhang, K. G. Zhou, K. F. Xie, J. Zeng, H. L. Zhang, Y. Peng, *Nanotechnology* **2010**, 21, 065201.
- [39] T. Hu, I. C. Gerber, *J. Phys. Chem. C* **2013**, 117, 2411.
- [40] S. Braun, W. R. Salaneck, M. Fahlman, *Adv. Mater.* **2009**, 21, 1450.
- [41] S. S. Qureshi, Z. Zheng, M. I. Sarwar, O. Félix, G. Decher, *ACS Nano* **2013**, 7, 9336.
- [42] P. L. Silvestrelli Van der, *Phys. Rev. Lett.* **2008**, 100, 053002.
- [43] J. Carrete, R. C. Longo, L. J. Gallego, A. Vega, L. C. Balbás, *Phys. Rev. B* **2012**, 85, 125435.
- [44] I. Hamada, *Phys. Rev. B* **2012**, 86, 195436.